Prediction of particle deposition on the walls of a cubical cavity with differentially heated opposed walls using heat and mass transfer laminar mixed convection boundary layer models

Jordi Pallares* and Alexandre Fabregat
Departament d'Enginyeria Mecànica. Universitat Rovira i Virgili.
Av. Països Catalans, 26. 43007-Tarragona. Spain
*Corresponding author: jordi.pallares@urv.cat

ABSTRACT

In this paper we present a model to predict particle deposition velocities on the isothermal walls bounding a turbulent natural convection flow at moderate Rayleigh numbers. The model is based on the laminar mixed convection characteristics of the velocity and thermal boundary layers near the thermally active walls of the cavity. These characteristics are verified with Direct Numerical Simulations reported elsewhere. The model considers the gravity force, the thermophoretic effect and the Brownian diffusion of small particles. The predicted deposition velocities are compared successfully with those obtained with one of the most popular particle deposition models and with experimental measurements reported in the literature and carried out in a cavity with the same thermal boundary conditions as those considered in this study.

Keywords: particle deposition, boundary layer, turbulent natural convection, thermophoresis, Brownian motion.

NOMENCLATURE

c	Concentration [kg m^{-3}]
C^*	Non-dimensional concentration, $C^* = c/c_\infty$, [-]
C_D	Drag coefficient [-]
C_c	Cunningham slip correction factor [-]
d	Diameter [m]
f	Non-dimensional streamfunction [-]
g	Gravity acceleration [m s^{-2}]
k	Thermal conductivity [W m^{-1} K^{-1}]
K_T	Non-dimensional temperature gradient at the wall [-]
K_{TP}	Thermophoresis constant [-]
K_v	Non-dimensional velocity gradient at the wall [-]
Re_p	Particle Reynolds number ($Re = \lvert U_p - U_f \rvert d_p/\nu$) [-]
Re_x	Local Reynolds number ($Re_x = U_\infty x/\nu$) [-]
k_B	Boltzmann constant [J K^{-1}]
D	Diffusion coefficient [m^2 s^{-1}]
Kn	Knudsen number ($Kn = 2\,\lambda/d_p$) [-]
L	Length of the cubical cavity [m]
Pr	Prandtl number ($Pr = \nu/\alpha$) [-]
Ra	Rayleigh number ($Ra = g\beta\Delta T L^3/\nu\alpha$) [-]
Re	Reynolds number ($Re = U_\infty L/\nu$) [-]
Sc	Schmidt number ($Sc = \nu/D$) [-]
t	Time [s]
T	Temperature [K]
U	Velocity [m s^{-1}]
u, v, w	Velocity components [m s^{-1}]
x, y, z	Cartesian coordinates [m]
Greek letters	
Δ	Increment [-]
ϵ	Perturbation parameter [-]
Ψ	Streamfunction [s^{-1}]

1	α	Thermal diffusivity [$m^2 \cdot s^{-1}$]
2	β	Thermal expansion coefficient [K^{-1}]
3	γ	Non-dimensional concentration [-]
4	η	Similarity variable [-]
5	θ	Non-dimensional temperature [-]
6	λ	Mean free path [m]
7	μ	Dynamic viscosity [$kg \cdot m^{-1}\ s^{-1}$]
8	ν	Kinematic viscosity [$m^2 \cdot s^{-1}$]
9	ρ	Density [$kg \cdot m^{-3}$]
10	τ	Time scale [s]
11	v	Deposition velocity [$m\ s^{-1}$]
12	*Subscripts*	
13	0	Forced convection contribution
14	1	Free convection contribution
15	∞	Value outside the boundary layer
16	C	Cold
17	f	Fluid
18	g	Gravitational settling
19	h	Horizontal
20	H	Hot
21	p	Particle
22	s	Settling
23	tp	Thermophoresis
24	T	Temperature
25	u	Velocity
26	v	Vertical
27	w	Wall
28	$\sim$	relative to the constant settling velocity
29		

1. INTRODUCTION

Enclosed turbulent natural convection flows can be found in many engineering applications such as nuclear reactors, solar collectors, refrigeration of electronic components and, among others, in indoor environments. Two canonical flow configurations, confined (heated from below) turbulent Rayleigh-Bénard flows (Ahlers et al. 2009; Chillà and Schumacher 2012) and confined heated from one sidewall (Saury et al. 2011, Trias et al. 2013, Miroshnichenko and Sheremet 2018), have been extensively analyzed to determine and understand the effect of the buoyancy induced flow on the wall heat transfer rates and the characteristics of the flow structures. Variations of these two prototypical situations in terms of the boundary conditions and geometries are countless. (See for example Pandey et al. 2019)

Particle dispersion in enclosed turbulent natural convection flows is of interest because it has implications in the air indoor quality (Lai, 2002) and in the fouling of art pieces in display cases in museums and exhibitions (Grau-Bové and Strlič, 2013). Micro-size aerosol particle deposition rates driven by natural convective flows inside large containments is of interest to assess the risks and the environmental impact of accidents in nuclear power plants (Kissane, 2008). The particle deposition flux onto surfaces is the result of the combined effect of different physical mechanisms and factors, such as turbulent and Brownian diffusion, thermophoresis, turbophoresis gravitational and electrostatic forces, particle aggregation and surface characteristics, that can contribute to the transport of the particles towards the wall (Liu, 2010; Elimelech et al. 2013).

Experiments of particle deposition produced by forced convection flows have been performed in enclosures (Thatcher et al. 2002, Wang et al. 2018, Cetin et al. 2020). However, numerical simulations and experiments of particle dispersion and deposition in enclosed natural convection flows are less frequent in the literature and have been conducted in side-heated cavities and, with less extension, in enclosures heated from below. Numerical simulations and particle Lagrangian tracking in the 2D square side heated cavity are reported in Puragliesi et al. (2011), Bagheri et al. (2012). Particle

dispersion and deposition in three-dimensional configurations are reported by Kalilanen et al. (2016), Dehbi et al. (2017) and Kim et al. (2018) who analyzed, using experiments and large-eddy simulations with one-way Lagrangian tracking, the particle deposition in a side-heated cubical cavity at $Ra \approx 10^9$ seeded with silica particles with diameters from 0.5 μm to 2.5 μm. The numerical predictions of the rate of the suspended particle depletion agree with the corresponding measurements. A similar numerical approach was used by Bosshard et al. (2014) to track larger particles 10 μm ≤ d_p ≤ 35 μm in a side-heated cubical cavity at $Ra = 10^9$. For these conditions gravitational settling was found the dominant deposition mechanism. The same flow configuration was used by Gereltbyamba and Lee (2018) at slightly lower Rayleigh numbers and particle diameters in the range 15 μm ≤ d_p ≤ 75 μm to analyze the regions of preferred deposition on the walls and the regions of particle depletion within the flow. The effect of the solid phase on the flow (two-way coupling) has been reported in the side-heated cubical cavity by Gereltbyamba and Lee (2019) and in Rayleigh-Bénard convection in a cylindrical container (Oresta and Prosperetti, 2013) and, recently, in a two-dimensional cavity heated from below (Xu et al. 2020).

Most of the analytical models to predict particle deposition are based on a modified Fick's law that relates the constant particle flux within the particle mass transfer boundary layer with the particle concentration gradient using the Brownian diffusivity of the particle and an eddy particle diffusivity (Corner and Pendlebury, 1951; Crump and Seinfeld, 1981, Lai and Nazaroff 2000). Several expressions to compute the eddy particle diffusivity have been proposed (Lai and Nazaroff 2000) and additional effects such as turbophoresis or the inclination of the surface can be relatively easily included in the flux equation (You et al. 2012, Zhao and Wu, 2007). An input to all these models is the friction velocity that characterizes the velocity gradient within the particle mass transfer boundary layer. The friction velocity is estimated from numerical simulations or obtained from fitting the model to experimental measurements.

In this study we center our attention in the particle deposition on the walls of an enclosed cavity with simultaneously imposed horizontal and vertical temperature gradients under turbulent regime. This arrangement of thermal boundary conditions,

often refereed as mixed cavity free convection, has the ingredients of the heated from below and heated from the side flow configurations with simultaneously hot and cold vertical and horizontal walls. The bottom wall and one vertical wall are heated at the same temperature, while opposite walls are kept at a lower temperature. The remaining other two sidewalls are considered adiabatic. In addition, for this flow configuration particle deposition measurements are available in the literature (Thatcher et al. 1996)

Experiments in a cubical cavity, with dimension L=30.5 cm and with this arrangement of thermal boundary conditions, filled with water at $4 \cdot 10^9 \leq Ra \leq 4.5 \cdot 10^{10}$ were performed by Kirkpatrick and Bohn (1986) to report the heat transfer rates, the visualization of the flow patterns and the measurements of the temperature distributions. Hanjalić and Vasić (1993) carried out simulations in a two-dimensional square cavity at $Ra = 2.15 \cdot 10^{10}$ solving numerically the Reynolds-Averaged Navier-Stokes equations. Direct Numerical Simulations (DNS) of the laminar and turbulent flow in a cubical cavity with differentially heated opposed walls are reported in Fabregat and Pallares (2020) for air ($Pr = 0.7$) in the range of Rayleigh numbers $10^5 \leq Ra \leq 5.4 \cdot 10^8$. At $Ra \geq 10^7$ the flow is turbulent and it consists in a large-scale circulation with ascending flow parallel and close to the vertical hot sidewall and descending flow near the vertical cold sidewall. As shown in Fabregat and Pallares (2020) at $Ra = 5.4 \cdot 10^8$ the boundary layers remain essentially laminar and the velocity and temperature profiles are well reproduced by classical laminar boundary layer models. The sense of rotation of this large flow structure, imposed by the thermal boundary conditions of the thermally active vertical walls, inhibits the reorientation of this main circulation around the vertical axis of the cavity observed in the cubical cavity heated from below (Vasiliev et al. 2019).

Thatcher et al. (1996) carried out experiments in the cubical cavity, with dimension L=1.22 m, filled with air at $Ra = 5.4 \cdot 10^8$ and $Ra = 3.6 \cdot 10^9$ to measure particle deposition rates on the horizontal and vertical thermally active smooth walls. The effect of the surface roughness in these experiments was analyzed in Thatcher and Nazaroff (1997). Solid ammonium fluorescein particles with diameters from 0.1 μm to

2.5 μm were released in the cavity and the mass of the deposited particles was measured in a series of surfaces distributed along the symmetry plane (z=0) of the vertical and horizontal thermally active walls. These measurements revealed the importance of thermophoresis in this range of particle sizes.

In this paper we analyze the predictions of the particle deposition rates of boundary layer models in a cubical cavity with differentially heated opposed walls at the same turbulent natural convection flow conditions used in the experiments of Thatcher et al. (1996). A brief description of the flow and the validity of the boundary layer approximations to predict velocity and temperature profiles near the walls are reported in Section 2. The mass transfer boundary layer models and the comparison with experiments are described in Section 3 and conclusions are outlined Section 4.

2. DNS AND BOUNDARY LAYER MODELS FOR VELOCITY AND TEMPERATURE

In this section we summarize the results of the DNS of the flow at $Ra = 5.4 \cdot 10^8$ ($Pr = 0.7$) and the velocity and temperature boundary layer models reported by Fabregat and Pallares (2020) relevant to the particle deposition model presented in this study. The schematic of the cubical cavity is shown in Figure 1.

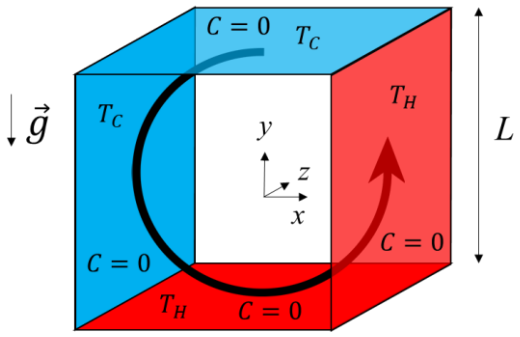

Figure 1. Schematic illustration of the cubical cavity.

Figure 2 shows the time averaged non-dimensional velocity contours on the vertical symmetry plane of the cavity ($z = 0$). The velocity scale used to obtain the dimensionless velocities is $\alpha Ra^{1/2}/L$. Although, as reported and discussed by Fabregat and Pallares (2020), at this Rayleigh number the time averaged flow is not completely

symmetric with respect to $z = 0$, the clockwise main large scale circulation can be seen in Fig. 2 and in Fig. 3, which shows the horizontal and vertical velocity components and the temperature profiles along the vertical and horizontal bisectors of the vertical symmetry plane of the cavity.

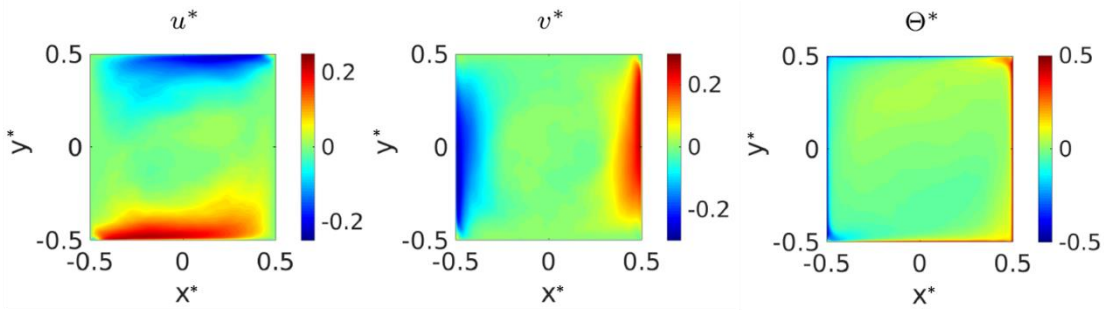

Figure 2. Time averaged contours of the non-dimensional horizontal and vertical velocity component and temperature on the plane z=0 at Ra=5.4·10^8 obtained with the DNS of Fabregat and Pallares (2020). The non-dimensional axis, velocities and temperatures are defined, respectively, as $x_i^* = x_i/L, u_i^* = u_i/(\alpha Ra^{1/2})$ and $\Theta^* = (T - T_0)/(T_H - T_C)$

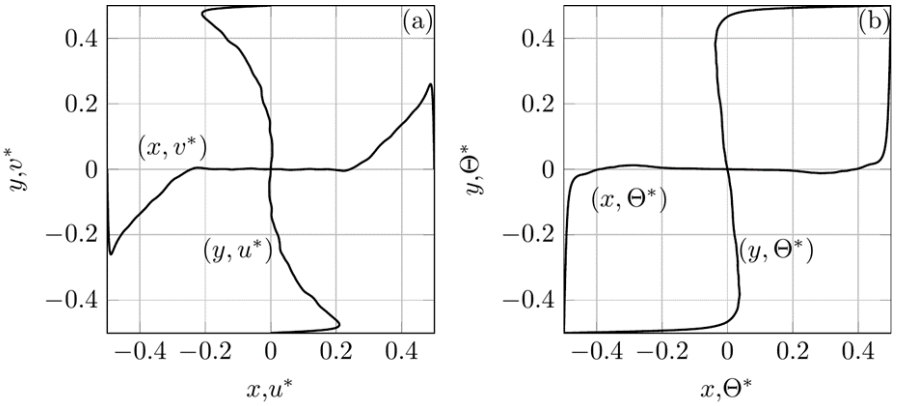

Figure 3. (a) Time averaged velocity and (b) temperature profiles along the bisectors of the plane z=0 at Ra=5.4·10^8 obtained with the DNS of Fabregat and Pallares (2020). See caption of Fig. 2 for the definition of the non-dimensional variables.

In what follows, irrespectively of the wall considered, we take the positive x-direction parallel to the wall along the direction of the main flow and the y-direction perpendicular to the wall, which is located at $y = 0$. The boundary layer models for velocities and temperature near the horizontal walls considered by Fabregat and Pallares (2020) consist in a forced convection boundary layer with a small perturbation produced by natural convection. This assumption was adopted successfully by Shi et al.

(2012) to analyze the horizontal boundary layers of turbulent Rayleigh-Bénard convection. According to this, the fluid velocities near the horizontal walls are

$$u = U_\infty [f_0' + \epsilon f_1'] \tag{1}$$

$$v = \frac{U_\infty}{2Re_x^{1/2}} [\eta_h f_0' - f_0 + \epsilon(\eta_h f_1' - 2f_1)] \tag{2}$$

where η_h is the similarity variable,

$$\eta_h = \frac{y}{x} Re_x{}^{1/2} \tag{3}$$

and $\epsilon \ll 1$ is the free convection perturbation parameter. In Eq. 2, Re_x is the local Reynolds number based on the local streamwise position along the wall and the constant velocity outside the boundary layer, U_∞. The temperature within the boundary layer can be written as

$$T = T_\infty + (T_w - T_\infty)[\theta_0 + \epsilon\theta_1] \tag{4}$$

The details and the associated boundary layer ordinary differential equations to obtain the dependent variables f_0, f_1, θ_0 and θ_1 can be found in Shi et al. (2012) or in Fabregat and Pallares (2020) and are not repeated here for brevity.

For the vertical walls the ascending and descending near-wall flows are modelled as mixed convection vertical boundary layers. In this case, the definitions of the similar variables are

$$f_0 = \frac{\Psi Re_L^{1/2}}{U_\infty L} \left(\frac{L}{x}\right)^{3/4} \tag{5}$$

$$\eta_v = \frac{y}{x} Re_x^{1/2} \left(\frac{x}{L}\right)^{1/4} \tag{6}$$

where Re_L=$U_\infty L/\nu$. The details of this formulation can be found in Merkin (2016) or in Fabregat and Pallares (2020).

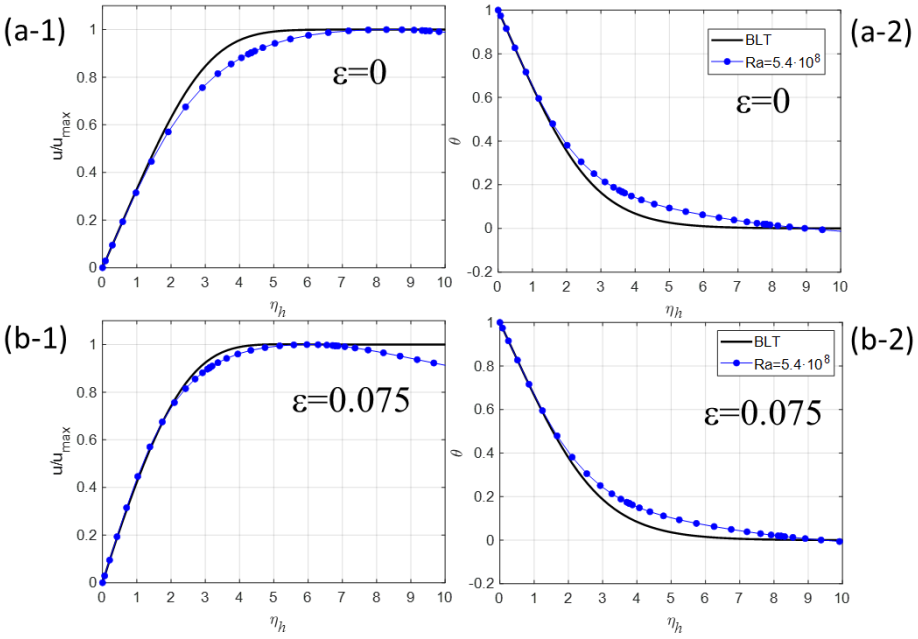

Figure 4. Comparison of the DNS time-averaged velocity and temperature profiles with the predictions of laminar mixed convection boundary layer models for the horizontal walls.

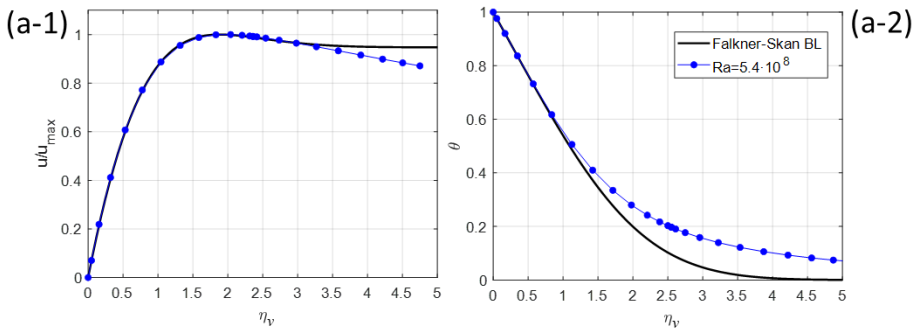

Figure 5. Comparison of the DNS time-averaged velocity and temperature profiles with the predictions of laminar mixed convection boundary layer models for the vertical walls.

The comparison of the time averaged numerical velocities and temperatures obtained from DNS, shown in Fig. 3, and the corresponding boundary layer predictions are plotted in Fig. 4 for the horizontal walls and in Fig. 5 for the vertical walls. It can be seen that, for the horizontal boundary layers, the introduction of a small contribution of buoyancy (Fig. 4b-1) into a pure forced convection boundary layer (Fig. 4a-1) improves the prediction of the numerically simulated velocities. In contrast,

temperature profiles (Figs. 4a-2 and 4b-2) are more insensitive to the value of the perturbation parameter ϵ. For the vertical boundary layers (Fig. 5), the mixed convection model, reproduce accurately the velocity profiles obtained from the simulation. In summary, Figs. 4 and 5 show that two-dimensional, mixed-convection, laminar boundary layer models can be used as good estimates of the flow for distances near the walls of $\eta < 2$ for velocities and of $\eta < 1$ for temperature.

DNS at $Ra = 5.4 \cdot 10^8$ revealed that the velocity boundary layer thickness of the horizontal and vertical boundary layers at the center of the corresponding walls are, respectively, about $\delta_h \approx 3 \cdot 10^{-3}\ L$ and $\delta_v \approx 4 \cdot 10^{-3}\ L$ (see Fig. 11 of Fabregat and Pallares, 2020). If we consider the physical dimension of the cavity used in the experiments of Thatcher et al. (1996) (L=1.22 m) and the diameter of the particles ($0.1\mu m \leq d_p \leq 2.5\mu m$) then the minimum ratio between the boundary layer thickness and the diameter of the particles ($3 \cdot 10^{-3}\ L\ /2.5 \cdot 10^{-6}$) is about $1.5 \cdot 10^3$. The ratio increases up to $4 \cdot 10^4$ for the smallest particles. This indicates that the deposition processes of these smallest particles with very small inertia ($St = \rho_p d_p^2 \alpha Ra^{1/2}/18\mu L^2 < 10^{-7}$) are governed, apart from gravity, by the flow and the temperature gradient within the boundary layer. At larger Rayleigh numbers, $Ra \approx 5 \cdot 10^9$, typical for natural convection flows of air with $\Delta T \approx 3\ K$ and $L \approx 3\ m$, the characteristic boundary layer thickness for velocity is $\delta_h \approx 10^{-3}\ L$ and the ratio of the velocity boundary layer thickness and the diameter of the largest particles in this case is maintained at $1.5 \cdot 10^3$. These considerations support the idea that, for the conditions considered, the relevant near wall flow and temperature distributions for the deposition of small particles (i.e. with very small inertia) can be modelled with the above boundary layer approximations.

3. MODEL AND DISCUSSION

3.1. Particle concentration mass transfer boundary layer models

We assume that the concentration of particles satisfies a steady two-dimensional boundary layer equation (Crowe et al. 2011). The advection terms contain the velocity of the particles and the diffusion term is due to the Brownian motion of the particles.

$$\frac{\partial u_p\, c}{\partial x} + \frac{\partial v_p\, c}{\partial y} = D\,\frac{\partial^2 c}{\partial y^2} \tag{7}$$

The local particle velocity is governed by the second Newton's law, which for $Re_p < 1$, ($C_D = 24/Re_p$ i.e. small spherical particles in creeping flow) can be written as,

$$\frac{d\vec{v}_p}{dt} = \frac{(\vec{v}-\vec{v}_p)}{\tau_p} + \left(1 - \frac{\rho}{\rho_p}\right)\vec{g} - \frac{18\mu^2 C_c}{\rho\,\rho_p\,d_p^2}\,K_{tp}\,\frac{\vec{\nabla}T}{T_\infty} \tag{8}$$

The different terms on the right-hand side of Equation 8 are, from left to right, the hydrodynamic drag force, the gravity force and the thermophoretic force. The accelerations originated from the pressure gradient force, the added mass force, the Basset force and the lift force, which are proportional to the ratio between the fluid density and the particle density are neglected in Eq. 8 since, for solid gas flows, $O(\rho/\rho_p)\sim 10^{-3}$. In Eq. 8 τ_p is the particle relaxation time (Crowe et al. 2011),

$$\frac{1}{\tau_p} = \frac{18\mu C_c}{\rho_p d_p^2} \tag{9}$$

and C_c is the Cunningham factor, which can be expressed as a function of the Knudsen number ($Kn = 2\,\lambda/d_p$) as (Allen and Raabe, 1982)

$$C_c = 1 + Kn[1.205\,exp(-0.0026/Kn) + 0.425\,\exp(-0.74/Kn)] \tag{10}$$

The value of K_{tp} in the thermophoretic force, for $Kn > 0.1$, can be computed as (Talbot et al. 1980),

$$K_{tp} = \frac{2C_s(k+2k_sKn)\left[1+2Kn\left(1.2+0.41\,exp(-0.44/Kn)\right)\right]}{(1+6C_mKn)(2k+k_s+4k_sC_tKn)} \tag{11}$$

with $C_s = 1.17$, $C_m = 1.14$ and $C_t = 2.18$.

Assuming small particles ($Re_p < 1$) and slow time varying fluid velocities within the boundary layer we can neglect the acceleration term on the left-hand side of Eq. 8 and the velocity of the particle can be computed as

$$\vec{v}_p = \vec{v} + \tau_p\left(1 - \frac{\rho}{\rho_p}\right)\vec{g} - \nu K_{tp}\frac{\vec{\nabla}T}{T_\infty} \tag{12}$$

The second term on the right-hand side of Eq. 12 corresponds to the constant gravitational settling velocity of the particles which can be absorbed into the velocity of the fluid.

$$\vec{v}_p = \vec{\tilde{v}} - \nu K_{tp}\frac{\vec{\nabla}T}{T_\infty} \tag{13}$$

Given the small particles considered we assume that the velocity component of the particles along the parallel to the wall direction is the same of that of the fluid. Then one can write, for the horizontal boundary layers

$$u_p = u;\; v_p = \tilde{v} - \nu\frac{K_{tp}}{T_\infty}\frac{\partial T}{\partial y} \tag{14}$$

and for the vertical boundary layers,

$$u_p = \tilde{u};\; v_p = v - \nu\frac{K_{tp}}{T_\infty}\frac{\partial T}{\partial y} \tag{15}$$

Note that, for horizontal boundary layers, the constant gravitational settling velocity is absorbed into the component of the fluid velocity vector perpendicular to the wall (Eq. 14) while for vertical boundary layers, into the component of the fluid velocity vector parallel to the wall (Eq. 15).

Similarly to the definition of the velocities (Eqs. 1 and 2) and temperature (Eq. 4), the non-dimensional concentration of particles can be defined as

$$c^* = \frac{c}{c_\infty} = \gamma_0 + \epsilon\gamma_1 \tag{16}$$

The introduction of Eqs. 1, 2, 4, 14 (or Eq. 15) and 16 in Eq. 7 results in

$$\gamma_0'' + Sc\frac{1}{2}f_0\gamma_0' + Sc\,\Delta T^* K_{tp}(\theta_0'\gamma_0' + \theta_0''\gamma_0) = 0 \tag{17}$$

Equation 17 is valid for both horizontal and vertical boundary layers because the particle velocity is relative to the constant settling velocity (see Eqs. 14 and 15). In Eq. 17, $Sc = \nu/D$ is the Schmidt number based on the Brownian diffusion coefficient of the particles, $D = k_B\bar{T}C_c/3\pi\mu d_p$, with $\bar{T} = (T_w + T_\infty)/2$ and $\Delta T^* = (T_w - T_\infty)/T_\infty$. Note that for the thermal boundary conditions considered in the physical model of the cavity (Fig. 1), $\Delta T^* = \pm\frac{(T_H - T_C)}{2T_\infty}$, where the sign on the right hand side is positive if one considers the hot walls and it is negative for the cold walls. The boundary conditions of Eq. 17 are at $\eta = 0$; $\gamma_0 = 0$ and at $\eta \to \infty$; $\gamma_0 = 1$. The first boundary condition assumes that the wall is a perfect sink for particles (i.e. no particle rebound or resuspension). As shown comparing Figures 4a-2 and 4b-2 the contribution of the buoyancy effect to the forced convection of the temperature profiles is very small (i.e. $\theta_0 \gg \epsilon\theta_1$, see Eq. 4). Particularly it can be seen a very small difference in the temperature profiles corresponding to a pure forced convection ($\epsilon = 0$, Fig. 4a-2) and those with a small buoyancy contribution ($\epsilon = 0.075$, Fig. 4b-2). Consequently, we neglected the buoyancy effect in the concentration (i.e. $\gamma_0 \gg \epsilon\gamma_1$), which satisfies a similar ordinary differential equation. The assumption of a constant and uniform concentration of particles outside the boundary layer is satisfied for small particles,

with small Stokes numbers, which do not exhibit regions with preferential particle concentration produced by the instantaneous turbulent flow structures within the large-scale circulation outside the boundary layers. For example, for the largest particles considered in the experiments of Thatcher et al. (1996) with $d_p = 2.5\mu m$, the Stokes number based on the maximum velocity of the boundary layers ($U \approx 0.06\ m/s$) is only 10^{-6}.

For the vertical walls the introduction of Eqs. 5, 6 and 15 into Eq. 7 results in

$$\gamma_0'' + Sc\frac{3}{4}f_0\gamma_0' + Sc\ \Delta T^* K_{tp}(\theta_0'\gamma_0' + \theta_0''\gamma_0) = 0 \tag{18}$$

Equations 17 and 18 can be expressed as

$$\gamma_0'' + Sc\ A\ f_0\gamma_0' + Sc\ \Delta T^* K_{tp}(\theta_0'\gamma_0' + \theta_0''\gamma_0) = 0 \tag{19}$$

with $A = \frac{1}{2}$ for horizontal boundary layers and $A = \frac{3}{4}$ for vertical boundary layers. In Eq. 19, f_0 and θ_0 are the corresponding solutions of the momentum and thermal energy boundary layer equations. The boundary conditions of Eq. 19 are at $\eta = 0$; $\gamma_0 = 0$ and at $\eta \to \infty$; $\gamma_0 = 1$.

Table I. Physical properties of the fluid and of the particles and parameters of the experiments of Thatcher et al. (1996)

Fluid					Particles	
ρ (kg·m^{-3})	β (K^{-1})	ν (m^2·s^{-1})	α (m^2·s^{-1})	k (W·m^{-1}·K^{-1})	ρ_p (kg·m^{-3})	k_p (W·m^{-1}·K^{-1})
1.3	$3.3\cdot10^{-3}$	$1.5\cdot10^{-5}$	$2.2\cdot10^{-5}$	$2.6\cdot10^{-2}$	1350	$4.3\cdot10^{-1}$

Cavity			
L (m)	T_H-T_C (K)	T_w-T_0 (K)	Ra
1.22	3	±1.5	$5.4\cdot10^{8}$
	20	±10	$3.6\cdot10^{9}$

3.2. *Comparison with experiments*

Tables I and II show the values of the relevant physical parameters for the conditions of the experiments carried out by Thatcher et al. (1996)

Table II. Parameters of the particles

d_p (μm)	Kn	C_c	Sc	K_{tp}	v_s (m/s)
0.1	1.36	2.95	$7.06\cdot10^{4}$	$2.47\cdot10^{-1}$	$1.22\cdot10^{-7}$
0.5	$2.72\cdot10^{-1}$	1.34	$3.53\cdot10^{5}$	$2.40\cdot10^{-1}$	$6.71\cdot10^{-6}$
0.7	$1.94\cdot10^{-1}$	1.24	$4.94\cdot10^{5}$	$2.38\cdot10^{-1}$	$1.42\cdot10^{-5}$
1.3	$1.05\cdot10^{-1}$	1.13	$9.18\cdot10^{5}$	$2.27\cdot10^{-1}$	$5.40\cdot10^{-5}$
2.5	$5.44\cdot10^{-2}$	1.07	$1.76\cdot10^{6}$	$2.05\cdot10^{-1}$	$2.12\cdot10^{-4}$

Because of the large values of the Schmidt number (see Table II), we assume linear velocity and temperature profiles within the concentration boundary layer and, thus,

$$f_0 = K_u \frac{\eta^2}{2};\ f_0' = K_u\,\eta;\ \theta_0 = K_T\,\eta \tag{20}$$

The solution of the momentum and thermal horizontal boundary layer equations for $Pr = 0.7$ gives $f_0''(\eta_h = 0) = K_u = 0.4613$ and $\theta_0'(\eta_h = 0) = K_T = -0.3321$. At the same Prandtl number and for vertical boundary layers the values are $K_u = 1.4854$ and $K_T = -0.4738$.

The introduction of these approximations into Equation 19 results in

$$\gamma_0'' + Sc\,\gamma_0'\left(\frac{A}{2}K_u\eta^2 + \Delta T^* K_{tp}\,K_T\right) = 0 \tag{21}$$

with the same boundary conditions as Eq. 19.

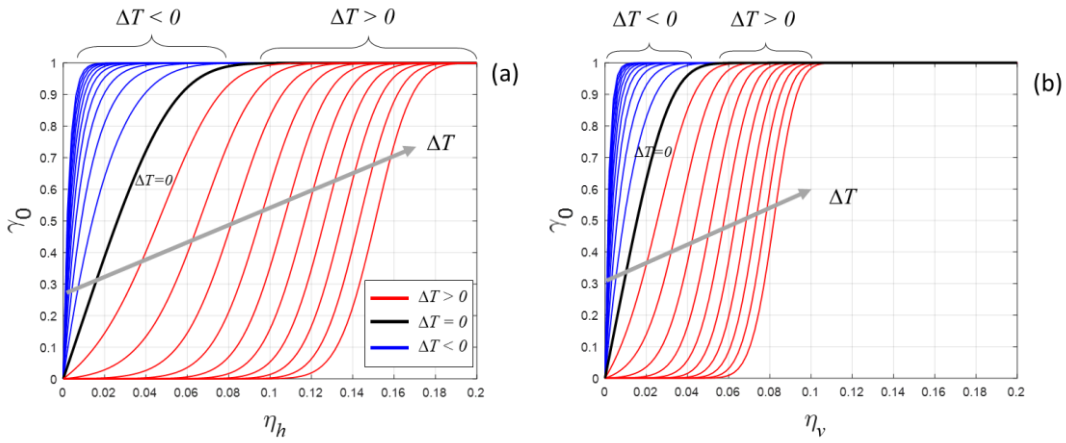

Figure 6. Non-dimensional concentration profiles for particles with the physical properties indicated in Table I and with diameter d_p=0.3 μm. The dimensional temperature increments range from $\Delta T = -10\ K$ to $\Delta T = 10\ K$ with an increment of $1\ K$. (a) Horizontal walls. (b) Vertical walls.

Figure 6 shows examples of the solution of Eq. 21 for horizontal (Fig. 6a) and for vertical (Fig. 6b) mass transfer boundary layers for different values of the dimensional temperature increment with $T_0 = 300\ K$ and for particles with a diameter of 0.3 μm. It can be seen that the mass transfer boundary layer thickness increases as the temperature increment increases because of the thermophoretic effect. For positive temperature increments the profiles exhibit an inflexion point and the wall mass flux density progressively decreases as the temperature increment increases. The location of this inflexion point can be determined setting to zero the term in parentheses of Eq. 21 and it can be written as

$$\eta_{\gamma_0''=0} = \left(\frac{-2\ \Delta T^* K_{tp}\ K_T}{A\ K_u}\right)^{1/2} \tag{22}$$

Note that since $K_T < 0$, Eq. 22 only gives real results for $\Delta T^* \geq 0$.

The local and the surface averaged deposition velocities of particles for horizontal boundary layers can be written as

$$v = D\ \frac{\partial C^*}{\partial y}\bigg|_{y=0} = D\ \gamma_0'|_{\eta_h=0}\ \frac{\partial \eta_h}{\partial y} = \gamma_0'|_{\eta_h=0}\ \frac{D\ Re_x^{1/2}}{x} = \gamma_0'|_{\eta_h=0}\ \frac{D\ U_\infty^{1/2}}{\nu^{1/2}\ x^{1/2}} \tag{23}$$

and

$$\bar{v} = \frac{1}{L}\int_0^L v\, dx = \gamma_0'|_{\eta_h=0}\frac{2\,D\,Re_L^{1/2}}{L} = \gamma_0'|_{\eta_h=0}\frac{2\,D\,U_\infty^{1/2}}{\nu^{1/2}\,L^{1/2}}, \tag{24}$$

respectively. Equation 24 corresponds to the deposition velocity produced by the Brownian motion and thermophoresis. The inclusion of the gravitational settling velocity to obtain the actual deposition velocity leads to

$$\bar{v} = MAX\left[\gamma_0'|_{\eta_h=0}\frac{2\,D\,Re_L^{1/2}}{L} \pm \tau_p\left(1-\frac{\rho}{\rho_p}\right)g, 0\right] \tag{25}$$

where the second term on the right-hand side of Eq. 25 is positive for horizontal walls facing up and negative for horizontal walls facing down. The MAX function sets the deposition velocity to zero for horizontal walls facing down when

$$\tau_p\left(1-\frac{\rho}{\rho_p}\right)g > \gamma_0'|_{\eta_h=0}\frac{2\,D\,Re_L^{1/2}}{L}. \tag{26}$$

For the vertical boundary layers the local and the surface-averaged deposition velocities are

$$v = D\left.\frac{\partial C^*}{\partial y}\right|_{y=0} = D\,\gamma_0'|_{\eta_v=0}\frac{\partial \eta_v}{\partial y} = \gamma_0'|_{\eta_v=0}\frac{D\,Re_x^{\frac{1}{2}}}{x}\left(\frac{x}{L}\right)^{\frac{1}{4}} = \gamma_0'|_{\eta_v=0}\frac{D\,U_0^{1/2}}{\nu^{1/2}\,x^{1/4}\,L^{1/4}} \tag{27}$$

and

$$\bar{v} = \gamma_0'|_{\eta_v=0}\frac{4\,D\,Re_L^{1/2}}{3\,L} = \gamma_0'|_{\eta_v=0}\frac{4\,D\,U_0^{1/2}}{3\,\nu^{1/2}\,L^{1/2}}, \tag{28}$$

respectively. Figure 7 shows the gradient of the nondimensional concentration at the wall ($\gamma_0'|_{\eta=0}$) for vertical (Fig. 7a) and horizontal (Fig. 7b) boundary layers of air ($Pr = 0.7$) for different particle diameters with the physical properties indicated in Table I and different temperature increments. It can be seen that the gradient of the non-dimensional concentration at the wall increases as the temperature increment

decreases and the particle diameter increases. In general, for a given temperature increment and particle diameter, the wall concentration gradient is larger for the vertical boundary layers than for the horizontal boundary layers.

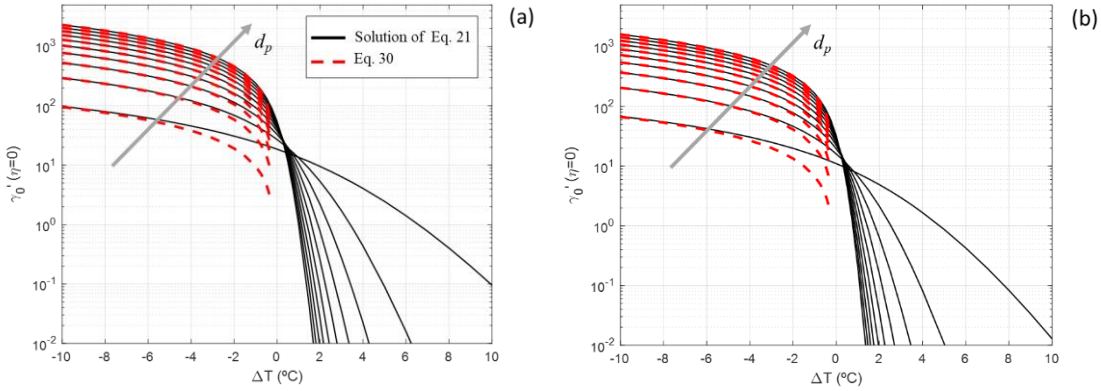

Figure 7. Gradient of the non-dimensional concentration of particles, with the physical properties indicated in Table I, at the wall ($\gamma_0'|_{\eta=0}$) for different particle diameters ranging from $d_p = 0.1\,\mu m$ to $d_p = 1\,\mu m$ with an increment of $\Delta d_p = 0.1\,\mu m$. Continuous lines are obtained with the solution of the mass transfer boundary layer equations (Eq. 19) and dashed lines correspond to the approximation given in Eq. 30. (a) Horizontal walls. (b) Vertical walls.

An approximate solution to Eq. 21 can be obtained if $\frac{K_v}{4}\eta^2 \ll \Delta T^* K_{tp}\, K_T$ (for example, with significant thermophoretic effects and very close to the wall). In this case the solution is

$$\gamma_0 \approx 1 - exp\left(-Sc\,\Delta T^* K_{tp}\, K_T \eta\right) = 0 \tag{29}$$

and the concentration gradient at the wall can be written as

$$\gamma_0'|_{\eta=0} \approx Sc\,\Delta T^* K_{tp}\, K_T \tag{30}$$

Note that this approximate expression is valid for $\Delta T^* \leq 0$ for which $\gamma_0'|_{\eta=0} > 0$ because $K_T < 0$. Figure 7 shows the approximation given by Eq. 30 that is plotted with dashed lines. It can be seen that this approximation is valid, for the particle diameters considered, for temperature increments smaller than -5ºC.

Equations 24 and 28 indicate that the deposition velocity depends on the Reynolds number based on the velocity out of the boundary layer. It can be seen in Figs. 2 and 3 that the maximum non-dimensional horizontal velocities are about 0.2 and the maximum vertical velocities are about 0.25. These scales can be used to compute the Reynolds number as a function of the Rayleigh number as

$$Re_L \approx 0.2 \frac{Ra^{1/2}}{Pr}, \tag{31}$$

The introduction of Eq. 31 into Equations 24 and 28 results in the following prediction of the deposition velocities for the horizontal walls

$$\bar{v} = MAX\left[\gamma_0'|_{\eta_h=0} \frac{0.894\, D\, Ra^{1/4}}{L\, Pr^{1/2}} \pm \tau_p \left(1 - \frac{\rho}{\rho_p}\right) g, 0\right] \tag{32}$$

and for the vertical walls

$$\bar{v} = \gamma_0'|_{\eta_v=0} \frac{0.667\, D\, Ra^{1/4}}{L\, Pr^{1/2}} \tag{33}$$

Figures 8 and 9 show, respectively, the predictions of the deposition velocities of Eq. 32 and 33 for horizontal and vertical walls as a function of the particle diameter. To make the curves more comparable we selected the following values $Ra = 5.4 \cdot 10^8$, $Pr = 0.7$, $L = 1.22\ m$ and the physical properties indicated in Table II.

Figure 8 shows the conventional behavior of the deposition velocity as a function of the particle diameter in horizontal surfaces. For very small particles ($d_p \approx 10^{-8} m$) the Brownian diffusion dominates the deposition process and, consequently, the deposition velocity decreases as the particle diameter increases because the Brownian diffusivity is inversely proportional to the particle diameter. For larger and more massive particles gravity enhances the deposition in upward horizontal surfaces (Fig. 8.a) and inhibits deposition in downward horizontal surfaces (Fig. 8.b). Figure 8 shows

that the thermophoretic effect decreases the deposition velocity as the temperature increment increases, as also indicated in Figure 7 considering the trend of $\gamma_0'|_{\eta=0}$ as ΔT is increased. The effect of thermophoresis is even more evident for vertical surfaces because gravity is perpendicular to the surface. As shown in Fig. 9 the deposition velocities for relatively large particles $d_p > 10^{-7}m$ is kept constant as the particle diameter is increased (i.e. reduction of the Brownian diffusivity) for negative temperature increments. Figure 9 shows that for positive temperature increments the deposition velocities are strongly reduced, especially for large temperature increments.

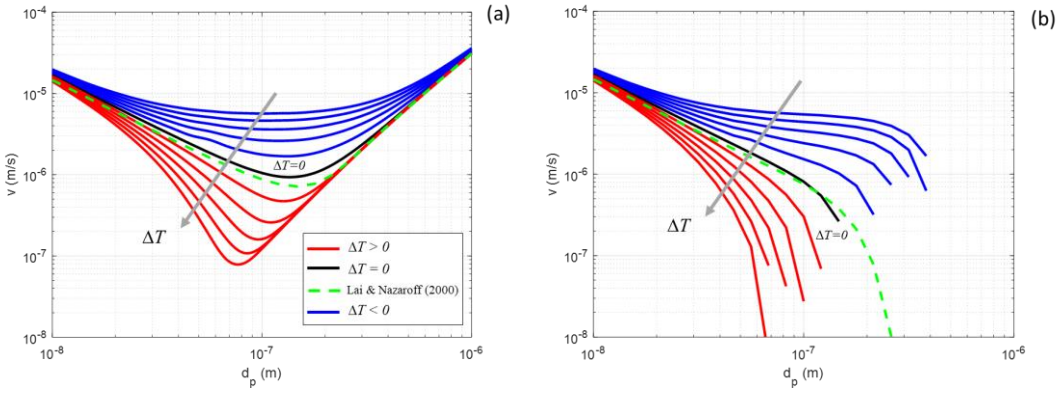

Figure 8. Deposition velocity onto horizontal surfaces for particles with the physical properties indicated in Table I. The dimensional temperature increments range from $\Delta T = -10\ K$ to $\Delta T = 10\ K$ with an increment of $2\ K$. (a) Horizontal upward walls. (b) Horizontal downward walls.

In Figures 8 and 9 we plotted with dashed lines the deposition velocities predicted by the model reported by Lai and Nazaroff (2000), which does not consider the thermophoresis effect ($\Delta T = 0$). For completeness, a brief description and the main hypotheses of this model are included in Appendix 1. It can be seen that the model by Lai and Nazaroff (2000) agrees with the present mixed convection boundary layer model, both, for vertical and horizontal walls. This indicates that, for the case considered the turbulent diffusivity, neglected in our mixed convection laminar boundary model, has a negligible contribution to the overall mass flux density (see Eq. A1 in Appendix 1).

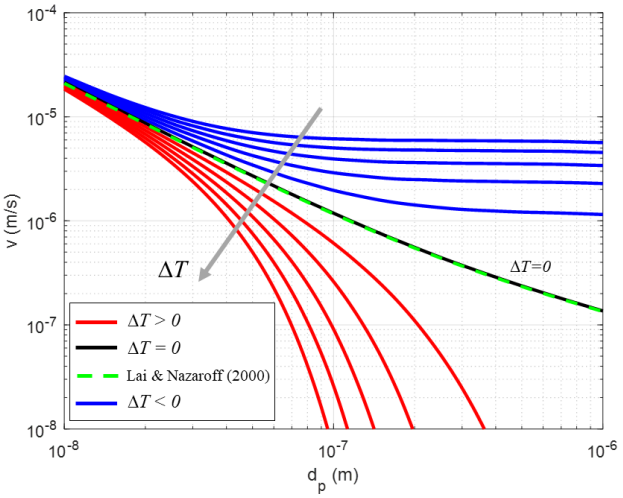

Figure 9. Deposition velocity onto vertical surfaces for particles with the physical properties indicated in Table I. The dimensional temperature increments range from $\Delta T = -10\ K$ to $\Delta T = 10\ K$ with an increment of $2\ K$.

Equations 32 and 33 have been used to predict the deposition velocities measured by Thatcher et al. (1996) in the four thermally active walls of the cavity. Figure 10 shows the comparison between the measurements and the model predictions. The horizontal axis corresponds to the location starting at the corner between the cold sidewall and the hot floor and continuing in the direction of the flow. Figure 10a corresponds to a temperature increment between the hot and cold walls of 3K ($Ra = 5.4 \cdot 10^8$) and Figure 10b, to 20K ($Ra = 3.6 \cdot 10^9$). The two sets of measurements, corresponding to two different experiments, for each wall are indicated with symbols. Dashed lines represent the detection limits and predictions obtained with the current model (Eqs. 32 and 33) are plotted with continuous red lines. In the plots corresponding to the bottom wall, we added the value of the settling velocity (see Table II) with dotted lines. Note that in some cases the predictions fall out of the vertical scale and they do not appear in the plots, as shown for the cold ceiling for $d_p \geq 0.5\ \mu m$ at $Ra = 5.4 \cdot 10^8$ and for $d_p \geq 0.7\ \mu m$ at $Ra = 3.6 \cdot 10^9$. In these cases, the settling velocities are much larger than the combined effect of the Brownian diffusion and thermophoresis, the first argument of the MAX function of Eq. 32 becomes negative and the model predicts zero particle deposition. For the hot vertical wall, the model also predicts negligible particle deposition because the thermophoresis effect is much larger than the Brownian diffusion. These situations for the larger particles, $d_p \geq 0.7\ \mu m$, correspond

to measurements close to the detection limits. Probably the fact that in the experiments measurements indicate a non-zero particle deposition is due to the unsteady character of the flow specially near the edges of the cavity that can transport, instantaneously, particles towards the wall.

However, it can be seen that the model reproduces the general features of the measurements. For the smallest particles ($d_p = 0.1\ \mu m$) the effect of the thermophoresis becomes more relevant at the largest Rayleigh number, with larger deposition velocities at the cold walls than at the hot walls. As the particle diameter is increased the effect of gravity reduces drastically the deposition on the top cold wall and increases the deposition on the floor. In fact, for $d_p \geq 0.5\ \mu m$ the model predicts a deposition velocity on the warm floor very close to the settling velocities. On the lateral walls, the increase of the particle diameter produces a reduction of the deposition, with larger deposition velocities on the cold sidewall than on the hot sidewall.

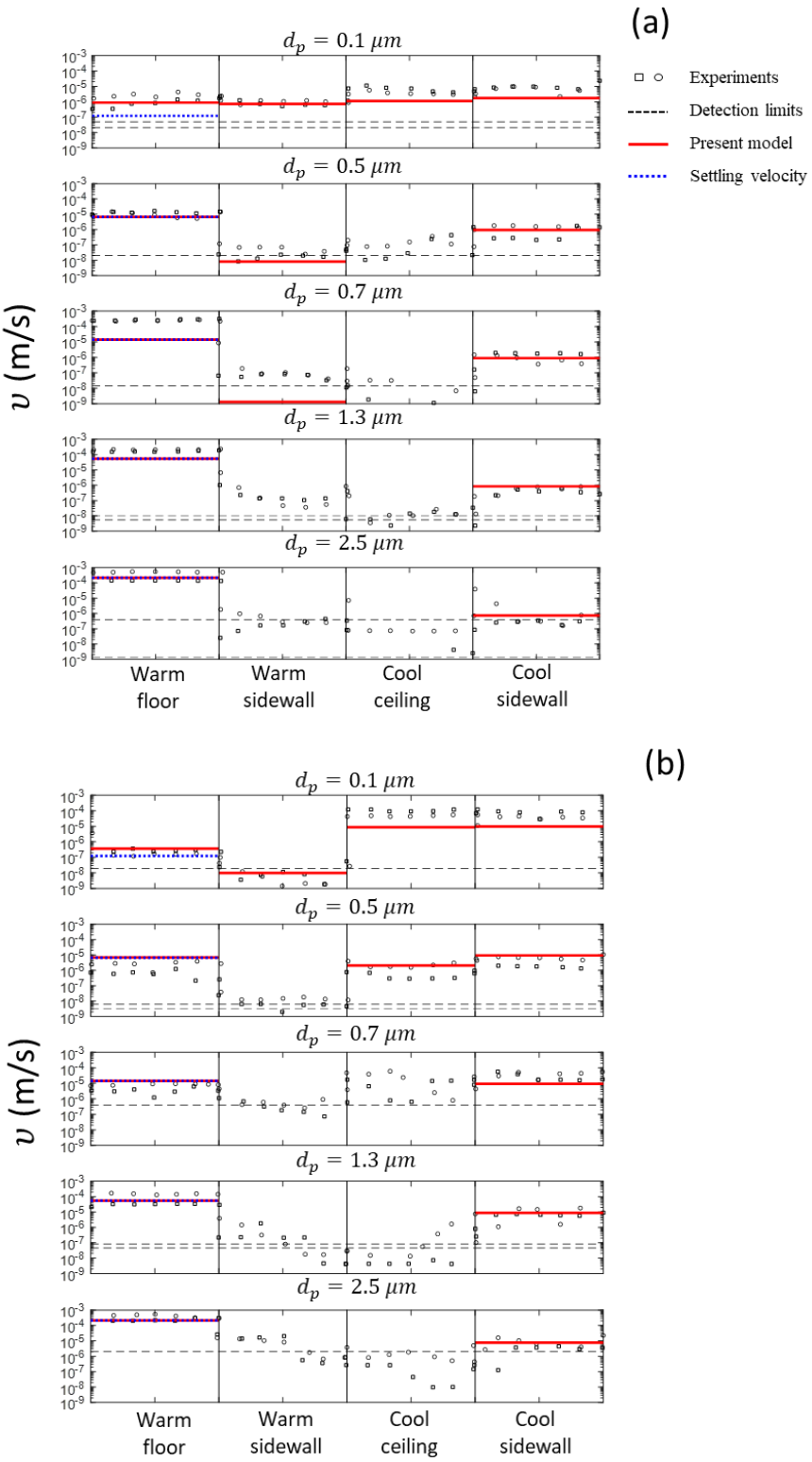

Figure 10. Comparison between the measured deposition velocities (symbols) and the model predictions (continuous lines). Circles and squares correspond to two different experiments. The experimental detection limits are indicated with dashed lines and the theoretical settling velocities given in Table II are plotted with dotted lines. (a) $T_w - T_0 = \pm 1.5\ K$, $Ra = 5.4 \cdot 10^8$. (b) $T_w - T_0 = \pm 10\ K$, $Ra = 3.6 \cdot 10^9$.

4. CONCLUSIONS

We developed a theoretical model to predict particle deposition velocities on the isothermal walls of an enclosed turbulent natural convection flow with differentially heated opposed walls. At moderate Rayleigh numbers $O(Ra)=10^8$-10^9, the boundary layers are laminar and are well approximated by classical two-dimensional mixed convection laminar boundary layers for velocity and temperature. For the horizontal walls, we considered forced convection boundary layers induced by the large-scale flow inside the cavity with a small contribution of buoyancy. Mixed convection Falkner-Skan boundary layers are used to model the vertical boundary layers. Considering this, we proposed a mass transfer boundary layer equation to predict the particle concentration within the velocity boundary layers. The equation takes into account gravity, Brownian diffusion and thermophoresis.

The predictions of the model are in agreement with existing general models for particle deposition rates onto smooth walls. A comparison with measurements available in the literature for the same flow configuration shows an overall agreement. Particularly, the model reproduces well the general trends observed in the experiments for different Rayleigh numbers and for different particle diameters.

The applicability of the model to other flow configurations, such as Rayleigh-Bénard convection or the canonical side-heated cavity, depends on the validity of the main assumptions of the model: (1) steady state two-dimensional laminar boundary layers (2) particles with small inertia and (3) particle deposition governed by gravity, Brownian diffusion and thermophoresis. For Rayleigh-Bénard flows the boundary layer approximation is valid at Rayleigh numbers ($Ra<10^{10}$) for which the large-scale flow is turbulent but the boundary layers, albeit fluctuating, remain laminar (Shi et al. 2012). Vertical boundary layers in side-heated cavities at large Rayleigh numbers exhibit strong fluctuations (Trias et al. 2010, Trias et al. 2013). This unsteadiness produces fluctuation intensities of the local Nusselt numbers between 30% and 50% specially in the near-wall region close to the leading edge of the boundary (see for example Fig. 1.e of Trias et al. 2010). The application of the model to these two boundary layers

with different behavior probably would produce reasonable predictions of particle deposition in Rayleigh-Bénard horizonal boundary layers. However, results are expected to be more limited for the vertical boundary layers of the side heated cavity.

Future research includes direct numerical simulations of the flow with particle tracking to analyze, locally, the spatial patterns of particle deposition on the walls and to investigate the effect on the deposition velocities of the unsteady fluid motions within the boundary layer that the model presented here does not take into account.

Acknowledgements

This work has been funded by Spanish Ministerio de Ciencia, Innovación y Universidades and FEDER through the grants DPI2016-75791-C2-1-P and RTI2018-100907-A-I00 and by the Generalitat de Catalunya through the grant 2017-SGR-1234.

APPENDIX 1

In this appendix we summarize the characteristics and main hypotheses of the particle deposition model reported by Lai and Nazaroff (2000). Perhaps, this model is one of the most used and, for example, it has been successfully applied to museum environments (Nazaroff et al. 1990).

In this model the mass flux density of particles (J) across a steady one-dimensional mass transfer turbulent boundary layer is assumed to be

$$J = -(D_T + D)\frac{dc}{dy} \tag{A1}$$

where D_T and D are is the turbulent and Brownian diffusivities. Under the assumption of a turbulent Schmidt number of one ($Sc_T = \nu_T/D_T \approx 1$) the model is based on the use of the conventional turbulent wall scaling, $y^+ = yu_\tau/\nu$ and the integration of Eq. A1 (i.e. constant mass flux density within the boundary layer) from the wall to $y^+ = 30$, where the concentration of particles is assumed to be equal to the bulk concentration. The variation of the turbulent diffusivity within the mass transfer boundary layer is taken from Direct Numerical Simulations of turbulent plane channel flow at a low Reynolds number (Kim et al. 1987). Finally, the non-dimensional deposition velocities, scaled with the friction velocity, can be expressed, for horizontal surfaces as

$$v^+ = \pm\frac{v_s^+}{exp(\pm v_s^+ I)-1} \tag{A2}$$

and for vertical surfaces as

$$v^+ = \frac{v_s^+}{I} \tag{A3}$$

In Equation A2, the plus signs correspond to upward surfaces and the minus signs to downward surfaces. The parameter I in these equations is a definite integral depending

on the molecular Schmidt number and on the particle radius expressed in wall coordinates (see Table 2 of Lai and Nazaroff, 2000)

The parameters of the model are the settling velocity (v_s), the diameter of the particles and the friction velocity, u_τ.

Our mixed convection laminar boundary layer approximations predict, for horizontal surfaces,

$$\left.\frac{du/u_\infty}{d\eta}\right|_{\eta=0} = K_u = 0.4613 \tag{A4}$$

and

$$\left.\frac{du/u_\infty}{d\eta}\right|_{\eta=0} = K_u = 1.4854 \tag{A5}$$

for the vertical surfaces.

The constant velocity outside the boundary layer is computed from Eq. 30 as,

$$u_\infty \approx 0.2\,\frac{\alpha Ra^{1/2}}{L} \tag{A6}$$

Introducing the definitions of the similar variable η (Eqs. 3 and 6) in Eqs. A4 and A5 to obtain the local friction velocity and integrating along the wall surface, the surface averaged friction velocities, for horizontal surfaces, can be expressed as,

$$u_\tau = 0.2873\,\frac{\nu^{1/4}\alpha^{3/4}Ra^{3/8}}{L} \tag{A7}$$

and for vertical surfaces

$$u_\tau = 0.4209\,\frac{\nu^{1/4}\alpha^{3/4}Ra^{3/8}}{L} \tag{A8}$$

The values of the friction velocity of Equations A7 and A8 have been used to compute the deposition velocities using Equations A2 and A3 plotted with dashed lines in Figures 8 and 9.

REFERENCES

Ahlers, G., Grossmann, S., & Lohse, D. (2009). Heat transfer and large scale dynamics in turbulent Rayleigh-Bénard convection. Reviews of modern physics, 81(2), 503.

Allen M.D., Raabe O. G. (1982) Re-evaluation of Millikan's oil drop data for the motion of small particles in air, Journal of Aerosol Science, 13(6), 537–547.

Bagheri G. H., Salmanzadeh M., Golkarfard V., Ahmadi G. (2012) Simulation of Solid Particles Behavior in a Heated Cavity at High Rayleigh Numbers, Aerosol Science and Technology, 46(12), 1382-1391.

Bosshard, C., Dehbi, A., Deville, M., Leriche, E., & Soldati, A. (2014). Large eddy simulation of particulate flow inside a differentially heated cavity. Nuclear Engineering and Design, 267, 154-163.

Cetin, Y. E., Avci, M., & Aydin, O. (2020). Particle dispersion and deposition in displacement ventilation systems combined with floor heating. Science and Technology for the Built Environment, 1-18.

Chillà, F., & Schumacher, J. (2012). New perspectives in turbulent Rayleigh-Bénard convection. The European Physical Journal E, 35(7), 58.

Corner, J., & Pendlebury, E. D. (1951). The coagulation and deposition of a stirred aerosol. Proceedings of the Physical Society. Section B, 64(8), 645.

Crowe, C. T., Schwarzkopf, J. D., Sommerfeld, M., & Tsuji, Y. (2011). Multiphase flows with droplets and particles. CRC press.

Crump, J. G., Flagan, R. C., & Seinfeld, J. H. (1982). Particle wall loss rates in vessels. Aerosol Science and Technology, 2(3), 303-309.

Dehbi, A., Kalilainen, J., Lind, T., & Auvinen, A. (2017). A large eddy simulation of turbulent particle-laden flow inside a cubical differentially heated cavity. Journal of Aerosol Science, 103, 67-82.

Elimelech, M., Gregory, J., & Jia, X. (2013). Particle deposition and aggregation: measurement, modelling and simulation. Butterworth-Heinemann.

Fabregat A. and Pallares J. (2020) Heat transfer and boundary layer analyses of laminar and turbulent natural convection in a cubical cavity with differently heated opposed walls. International Journal of Heat and Mass Transfer, 151, 119409.

Gereltbyamba, B., & Lee, C. (2018). Behavior of settling inertial particles in a differentially heated cubic cavity at moderate Rayleigh number. Journal of Mechanical Science and Technology, 32(7), 3169-3182.

Gereltbyamba, B., & Lee, C. (2019). Flow modification by inertial particles in a differentially heated cubic cavity. International Journal of Heat and Fluid Flow, 79, 108445.

Grau-Bové J. and Strlič M. (2013). Fine particulate matter in indoor cultural heritage: a literature review. Heritage Science, 1(1), 8.

Hanjalić K. and Vasić S. (1993) Computation of turbulent natural convection in rectangular enclosures with an algebraic flux model. International Journal of Heat and Mass Transfer, 36(14):3603-3624.

Kalilainen, J., Rantanen, P., Lind, T., Auvinen, A., & Dehbi, A. (2016). Experimental investigation of a turbulent particle-laden flow inside a cubical differentially heated cavity. Journal of Aerosol Science, 100, 73-87.

Kim, H., Dehbi, A., & Kalilainen, J. (2018). Measurements and LES computations of a turbulent particle-laden flow inside a cubical differentially heated cavity. Atmospheric Environment, 186, 216-228.

Kim, J., Moin, P., & Moser, R. (1987). Turbulence statistics in fully developed channel flow at low Reynolds number. Journal of fluid mechanics, 177, 133-166.

Kirkpatrick A. T. and Bohn M. (1986) An experimental investigation of mixed cavity natural convection in the high Rayleigh number regime, International Journal of Heat and Mass Transfer, 29(1):69-82.

Kissane, M. P. (2008). On the nature of aerosols produced during a severe accident of a water-cooled nuclear reactor. Nuclear Engineering and Design, 238(10), 2792-2800.

Lai A. C. (2002). Particle deposition indoors: a review. Indoor air, 12(4), 211-214.

Lai, A. C., & Nazaroff, W. W. (2000). Modeling indoor particle deposition from turbulent flow onto smooth surfaces. Journal of aerosol science, 31(4), 463-476.

Liu, D. L. (2010). Particle deposition onto enclosure surfaces. In Developments in Surface Contamination and Cleaning (pp. 1-56). William Andrew Publishing.

Merkin J. H. (2016) Mixed convection in a Falkner–Skan system, Journal of Engineering Mathematics, 100(1):167-185.

Miroshnichenko, I. V., & Sheremet, M. A. (2018). Turbulent natural convection heat transfer in rectangular enclosures using experimental and numerical approaches: A review. Renewable and Sustainable Energy Reviews, 82, 40-59.

Nazaroff, W. W., Ligocki, M. P., Ma, T., & Cass, G. R. (1990). Particle deposition in museums: comparison of modeling and measurement results. Aerosol Science and Technology, 13(3), 332-348.

Oresta, P., & Prosperetti, A. (2013). Effects of particle settling on Rayleigh-Bénard convection. Physical Review E, 87(6), 063014.

Pandey S., Park Y. G. and Ha M. Y. (2019) An exhaustive review of studies on natural convection in enclosures with and without internal bodies of various shapes, International Journal of Heat and Mass Transfer, 138, 762-795.

Puragliesi, R., Dehbi, A., Leriche, E., Soldati, A., Deville, M. O. (2011). DNS of buoyancy-driven flows and Lagrangian particle tracking in a square cavity at high Rayleigh numbers. International Journal of Heat and Fluid Flow, 32(5), 915-931.

Saury D., Rouger N., Djanna F. and Penot F. (2011). Natural convection in an air-filled cavity: Experimental results at large Rayleigh numbers. International Communications in Heat and Mass Transfer, 38(6), 679-687.

Shi N., Emran M. S. and Schumacher J. (2012) Boundary layer structure in turbulent Rayleigh-Bénard convection, Journal of Fluid Mechanics, 706:5-33.

Talbot, L., Cheng, R. K., Schefer, R. W., Willis, D. R. (1980). Thermophoresis of particles in a heated boundary layer. Journal of Fluid Mechanics, 101(4), 737-758.

Thatcher T. L., Fairchild W. A. and Nazaroff W. W. (1996) Particle deposition from natural convection enclosure flow onto smooth surfaces, Aerosol Science and Technology, 25(4), 359-374.

Thatcher, T. L., and Nazaroff, W. W. (1997). Effect of small-scale obstructions and surface textures on particle deposition from natural convection flow. Aerosol Science and Technology, 27(6), 709-725.

Thatcher, T. L., Lai, A. C., Moreno-Jackson, R., Sextro, R. G., & Nazaroff, W. W. (2002). Effects of room furnishings and air speed on particle deposition rates indoors. Atmospheric environment, 36(11), 1811-1819.

Trias, F. X., Gorobets, A., Oliva, A. and Pérez-Segarra, C. D. (2013). DNS and regularization modeling of a turbulent differentially heated cavity of aspect ratio 5. International journal of heat and mass transfer, 57(1), 171-182.

Trias, F. X., Gorobets, A., Soria, M., & Oliva, A. (2010). Direct numerical simulation of a differentially heated cavity of aspect ratio 4 with Rayleigh numbers up to 1011–Part II: Heat transfer and flow dynamics. International Journal of Heat and Mass Transfer, 53(4), 674-683.

Vasiliev A., Frick P., Kumar A., Stepanov R., Sukhanovskii A. and Verma M. K. (2019). Transient flows and reorientations of large-scale convection in a cubic cell. International Communications in Heat and Mass Transfer, 108, 104319.

Wang, Y., Fan, X., Li, A., Shang, L., & Wang, H. (2018). Deposition of fine particles on vertical textile surfaces: A small-scale chamber study. Building and Environment, 135, 308-317.

Xu, A., Tao, S., Shi, L., & Xi, H. D. (2020). Transport and deposition of dilute microparticles in turbulent thermal convection. Physics of Fluids, 32(8), 083301.

You, R., Zhao, B., & Chen, C. (2012). Developing an empirical equation for modeling particle deposition velocity onto inclined surfaces in indoor environments. Aerosol Science and Technology, 46(10), 1090-1099.

Zhao, B., & Wu, J. (2007). Particle deposition in indoor environments: analysis of influencing factors. Journal of hazardous materials, 147(1-2), 439-448.

FIGURE CAPTIONS

Figure 1. Schematic illustration of the cubical cavity.

Figure 2. Time averaged contours of the non-dimensional horizontal and vertical velocity component and temperature on the plane z=0 at Ra=5.4·10^8 obtained with the DNS of Fabregat and Pallares (2020). The non-dimensional axis, velocities and temperatures are defined, respectively, as $x_i^* = x_i/L, u_i^* = u_i/\left(\alpha Ra^{1/2}\right)$ and $\Theta^* = (T - T_0)/(T_H - T_C)$

Figure 3. (a) Time averaged velocity and (b) temperature profiles along the bisectors of the plane z=0 at Ra=5.4·10^8 obtained with the DNS of Fabregat and Pallares (2020). See caption of Fig. 2 for the definition of the non-dimensional variables.

Figure 4. Comparison of the DNS time-averaged velocity and temperature profiles with the predictions of laminar mixed convection boundary layer models for the horizontal walls.

Figure 5. Comparison of the DNS time-averaged velocity and temperature profiles with the predictions of laminar mixed convection boundary layer models for the vertical walls.

Figure 6. Non-dimensional concentration profiles for particles with the physical properties indicated in Table I and with diameter d_p=0.3 μm. The dimensional temperature increments range from $\Delta T = -10\ K$ to $\Delta T = 10\ K$ with an increment of $1\ K$. (a) Horizontal walls. (b) Vertical walls.

Figure 7. Gradient of the non-dimensional concentration of particles, with the physical properties indicated in Table I, at the wall ($\gamma_0'|_{\eta=0}$) for different particle diameters ranging from $d_p = 0.1\ \mu m$ to $d_p = 1\ \mu m$ with an increment of $\Delta d_p = 0.1\ \mu m$. Continuous lines are obtained with the solution of the mass transfer boundary layer

equations (Eq. 19) and dashed lines correspond to the approximation given in Eq. 30. (a) Horizontal walls. (b) Vertical walls.

Figure 8. Deposition velocity onto horizontal surfaces for particles with the physical properties indicated in Table I. The dimensional temperature increments range from $\Delta T = -10\ K$ to $\Delta T = 10\ K$ with an increment of $2\ K$. (a) Horizontal upward walls. (b) Horizontal downward walls.

Figure 9. Deposition velocity onto vertical surfaces for particles with the physical properties indicated in Table I. The dimensional temperature increments range from $\Delta T = -10\ K$ to $\Delta T = 10\ K$ with an increment of $2\ K$.

Figure 10. Comparison between the measured deposition velocities (symbols) and the model predictions (continuous lines). Circles and squares correspond to two different experiments. The experimental detection limits are indicated with dashed lines and the theoretical settling velocities given in Table II are plotted with dotted lines. (a) $T_w - T_0 = \pm 1.5\ K$, $Ra = 5.4 \cdot 10^8$. (b) $T_w - T_0 = \pm 10\ K$, $Ra = 3.6 \cdot 10^9$.